Hybrid Coupling Mechanism in a System Supporting High Order Diffraction, Plasmonic, and Cavity Resonances

Abraham Vázquez-Guardado,[1,2] Alireza Safaei,[3,2] Sushrut Modak,[1,2]
Daniel Franklin,[3,2] and Debashis Chanda[1,3,2,*]

[1]*CREOL, College of Optics and Photonics, University of Central Florida, Orlando, Florida 32816, USA*
[2]*NanoScience Technology Center, University of Central Florida, Orlando, Florida 32826, USA*
[3]*Department of Physics, University of Central Florida, Orlando, Florida 32816, USA*

The interactions between plasmonic and photonic modes of a cavity-coupled plasmonic crystal are studied in diffraction and diffractionless regimes, which lead us to the understanding of coherent interactions between electron plasma, higher order cavity, and diffraction modes. The strong interaction between plasmonic and photonic modes is shown to enhance as well as suppress surface plasmon resonance based on cavity phase relation. Numerical and analytical approaches are developed to accurately explain the physics of the interactions evident in their characteristic dispersion graphs. Further experimental measurements confirm the theoretical predictions.

The collective oscillation of free electrons coupled to electromagnetic radiation is fundamental to plasmonic-based devices. Apart from propagating surface plasmon-polaritons (SPP) present on dielectric-metal interfaces [1,2], isolated and periodic nanoparticles support localized surface plasmon resonances (LSPR) [3–6]. The resulting large field enhancement and tightly confined has been exploited in a plethora of applications such as surface-enhanced Raman spectroscopy [7–9], biosensing [10–13], reflective [14,15] and transmissive [16–18] optical filters, and vacuum Rabbi oscillations [19–21]. In addition, extraordinary optical transmission, attributed to LSPR and SPP, has been observed in sub-wavelength metallic hole arrays [22–26]. Recently, strong coupling between plasmonic and photonic modes has been demonstrated in hybrid LSPR Fabry-Perot (FP) cavities making use of near- and far-field interaction. In these cavity-coupled systems, three distinct configurations were previously studied where the plasmonic element is placed inside [27,28], at the front end [29–31] and at both ends [32–35] of the cavity. In the first configuration, coupling is studied from a cavity-atom picture in quantum electrodynamics based on the coupled oscillator model. However, the model suffers from the limitation in estimating the coupling coefficient, which is kept as a fitting parameter [27,28]. In the second and third cases, coupling has been studied theoretically using the Fourier modal [29,32], scattering matrix [34–36], numerical finite-difference time domain (FDTD) method [30,32], and finite integration technique [33] as a function of cavity length. The presence of a cavity influences surface plasmon excitation constructively or destructively, resulting in strong LSPR enhancement or complete suppression [27,30,37] purely by far-field interaction. However, the true nature and origin of this plasmonic-photonic interaction is yet to be understood in systems where higher order diffraction, LSPR, and cavity resonances overlap in space and frequency. Moreover, an analytical explanation describing the coupling mechanism is missing from the present literature.

In this Letter, we employ the analytical effective index and transfer matrix approaches in conjunction with the FDTD computational method to broaden the fundamental understanding of several far-field interaction mechanisms present within the characteristic dispersion of a cavity-coupled plasmonic system. Two scenarios are considered: when the coupled system supports diffraction orders and when it does not. Analytical design rules are developed, which avoids design optimizations based on tedious previously reported numerical simulations [27,30,32]. Further experimental results based on large area nanoimprint lithography and transfer printing solidify the theoretical conclusions and open up possibilities for novel cavity-based devices exploiting this strong plasmonic-photonic coupling.

The system is comprised of a dielectric slab of variable thickness L and refractive index n_d of 1.56 sandwiched between an optically thick (200 nm) gold back reflector and a patterned thin film of gold (30 nm). The thin film is perforated with 500 nm diameter holes arranged in a square array of period 740 nm as illustrated in Fig. 1(a). This choice of period and nanohole diameter ensures the excitation of higher diffraction orders as well as LSPR over the same near-IR spectral range [3,38–40]. The appropriate choice of cavity thickness further enables the overlap of FP cavity resonances with the LSPR. However, at subwavelength cavity thickness ($L < \lambda/2$), the incident light cannot create a photonic cavity mode, unlike the regime ($L > \lambda/2$) studied in this Letter. While each of these
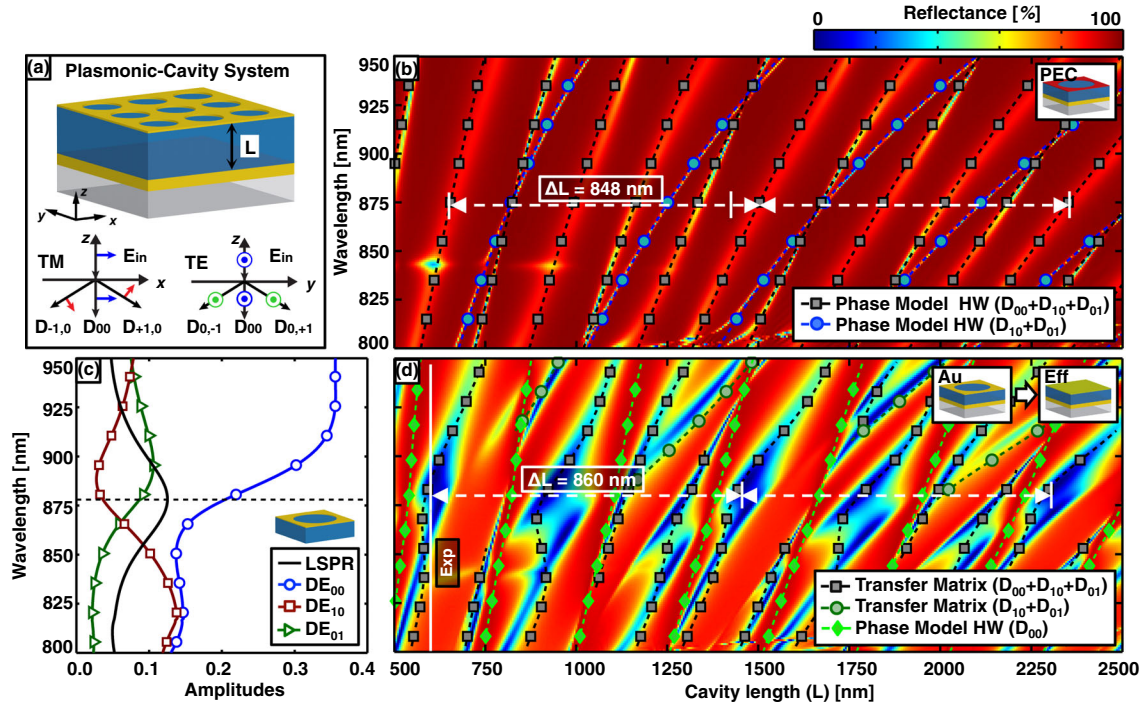
FIG. 1 (color online).   (a) Schematic representation of the studied plasmonic-cavity system in the presence of diffraction. (b) FDTD predicted reflectance spectra for a cavity with top PEC grating. Analytical predictions from the phase model have been overlaid on top. (c) Absorption spectrum (black line) for the perforated gold film showing a LSPR at $\lambda = 879$ nm and diffraction efficiencies for the fundamental D_{00} (blue circles) and first-order modes D_{10} (red squares) and D_{01} (green triangles). (d) FDTD predicted reflectance spectra for the cavity with a top gold pattern. Analytical predictions from the transfer matrix method and phase model have been overlaid on top.

physical phenomena is individually well understood, systems that incorporate all three lead to complex behavior.

To elucidate the optical properties of such a system, we begin with the general absorption enhancement of homogenous weakly absorbing materials in asymmetric cavities (i.e., dissimilar reflectivity at both ends) [41]. Such absorption is maximized when the top film is located at a quarter wave (QW) distance (antinode) from the back reflector due to constructive phase addition between incident and reflected light. Weak absorption is observed when the film is located at half-wavelength (HW) distance (node) from the back reflector corresponding to a FP mode. The general round-trip phase condition for strong absorption satisfies

$$2\phi - \rho_{BM} - \rho_F = 2\pi\left(s + \frac{1}{2}\right), \tag{1}$$

where ϕ is the longitudinal propagation phase in the cavity, ρ_{BM} and ρ_F are the reflection phases at the back mirror and top film, respectively, and s is an integer denoting the order of the resonance. For the present case, the periodic two-dimensional (2D) metallic grating introduces higher order diffracted light into the cavity whose propagation wave vector satisfies the well-known grating dispersion equation

$$\left(m\frac{2\pi}{P}\right)^2 + \left(n\frac{2\pi}{P}\right)^2 + k_{mnz}^2 = k_0^2 n_d^2, \tag{2}$$

where P is the array period, k_{mnz} is the longitudinal wave vector component, k_0 is the wave vector magnitude in vacuum, and (m, n) are the diffraction order indices (D_{mn}). Between the wavelengths of 840 to 1100 nm, at normal angle of incidence, the 2D grating supports the fundamental and first diffraction orders, denoted by D_{00}, $D_{\pm 10}$, and $D_{\pm 01}$ respectively. For notational simplicity, symmetric diffraction orders are indicated as $D_{-10} = D_{+10} = D_{10}$ and $D_{-01} = D_{+01} = D_{01}$. In our chosen geometrical configuration and incident light polarization, as seen in Fig. 1(a), D_{01} and D_{10} are twofold degenerate transverse electric (TE) and transverse magnetic (TM) modes, respectively.

In order to isolate the effect of diffraction and surface plasmons over the chosen wavelength range, the top metal is replaced by a perfect electric conductor (PEC), which ensures the absence of surface plasmons as well as surface modes that can affect the diffracting characteristic of the grating [42,43]. Diffraction orders with finite longitudinal wave vector and transverse electric field components coexist and interfere in the cavity. The fundamental and first-order modes possess different longitudinal wave vectors and experience different propagation phases for the same cavity length. The first-order modes D_{01} and D_{10} interfere constructively when the phase satisfies the following condition:

$$2k_{1z}L - \phi_1 = 2\pi q, \tag{3}$$

where $k_{1z} = k_{10z} = k_{01z}$, q is a multiple integer, and $\phi_1 = \phi_{01\mathrm{BM}} + \phi_{01F} + \phi_{10\mathrm{BM}} + \phi_{10F}$ is the total phase accumulated for the (m, n)th order from reflections off the top film (ϕ_{mnF}) and back mirror ($\phi_{mn\mathrm{BM}}$) interfaces. The fundamental and first-order modes D_{00}, D_{10}, and D_{01} interfere constructively when the phase condition becomes

$$2(k_{00z} + k_{1z})L - \phi_{00} - \phi_1 = 2\pi l, \qquad (4)$$

where l is a integer multiple, k_{00z} is the longitudinal wave vector and $\phi_{00} = \phi_{00\mathrm{BM}} + \phi_{00F}$ is the total phase due to the reflection at the top film and back mirror for D_{00}. The reflectance spectra for cavity thicknesses spanning from 500 nm to 2.5 μm were calculated using FDTD for x-polarized light as shown in Fig. 1(b). The cavity thickness range was chosen in order to support photonic modes inside the cavity for the chosen wavelength range. Because of the absence of plasmon resonances on the patterned PEC film, Fig. 1(b) purely captures cavity modes induced by diffraction. An experimentally fitted dispersion was used for a gold back mirror based on a two-pole Lorentzian Drude model [44]. On top of the FDTD color plot, the closed form dispersion curves for the HW condition are plotted for the combined D_{10} and D_{01} orders (circle, dashed blue line) as described by Eq. (3) and the combination of D_{00}, D_{10}, and D_{01} (square, dashed black line) as defined by Eq. (4). In the analytical phase model, the phase upon reflection from the top film for all diffraction orders is considered π for the PEC case whereas the phase from reflection on the gold back mirror was calculated from the Fresnel coefficients for the appropriate polarization and wavelength-dependent angle of incidence for the first diffraction order. Dips in reflectance are observed as light is coupled into resonant waveguide modes. The complex dispersion pattern is periodic in nature and repeats every 848 nm for the chosen example, which is governed by the periodicity of the top nanohole array. The aforementioned intracavity multiple beam interference that originates in the absence of plasmon resonance is exploited to identify the interaction between diffraction orders and their spectral dispersion in real metals.

To simulate the real system, the PEC top nanohole array is replaced with a patterned gold film, which introduces plasmon resonances to the system as a perturbation. In order to identify the location of the LSPR mode, the reflectance (R) and transmittance (T) of the patterned film on the dielectric are calculated from FDTD. The absorption is estimated by $A(\lambda) = 1 - R(\lambda) - T(\lambda)$ and shown in Fig. 1(c) (black curve). Electric field distributions (Fig. S1 of the Supplemental Material [45]) clearly show a predominantly dipolar LSPR corresponding to the absorption peak at 879 nm. Diffraction efficiencies computed from far-field projection of the transmission spectrum are also plotted in Fig. 1(c), indicating wavelength-dependent relative strengths of major diffraction orders (D_{00}, D_{01}, and D_{10}). Three distinct interaction

regions between 800 and 950 nm wavelength range can be observed and are defined by the relative strength of the diffraction orders. In region one, between 800 and 850 nm, D_{10}'s strength is comparable to D_{00}'s while D_{01} is roughly an order of magnitude smaller. In the second region, D_{00} is dominant over the 900 to 950 nm wavelength band. In the third transition region, around 875 nm, the TM mode D_{10} experiences extinction due to LSPR excitation, unlike its TE counterpart D_{01}. The complete system reflectance spectra are calculated using FDTD for the same wavelength and cavity thickness range, as shown in Fig. 1(d) (for near-field coupling see Fig. S3(a) in the Supplemental Material [45]). The LSPR, being an electromagnetic-field-driven process, is strongly influenced by the photonic mode when both overlap in space and frequency. Intuitively, one would expect a continuous absorption line across the cavity length due to the unperturbed top gold pattern that defines the LSPR. However, interestingly a discrete set of high absorption points is observed [Fig. 1(d)] in the present coupled system due to constructive or destructive interferences of the resultant electric field excitation, which enhances or suppresses the LSPR based on the cavity phase relation (controlled by cavity thickness). This mode hybridization can be observed in Fig. S7 (Supplemental Material [45]) where the isolated Fabry-Perot, the LSPR on the patterned film, and the coupled system pictorially show the mode hybridization process. The periodic modulation of the cavity-dependent dispersion of LSPR differs among the first three events and repeats periodically every 860 nm as cavity thickness increases, a fact pointed out previously in the PEC case. However, the simple analytical phase model, which accurately predicted the dispersion in the PEC case, is inadequate due to the complex phase retardation on the perforated gold film in the presence of LSPR. In order to quasianalytically model and predict this intricate resonance dispersion, we employ an approach based on the effective index and transfer matrix methods [41]. The perforated metal film is replaced with a uniform layer of equivalent wavelength-dependent effective index obtained by inverting Fresnel transmission and reflection coefficients [46–48] (for a detailed description see the Supplemental Material [45]). Following the transfer matrix approach, the reflectance spectra produced by the multilayer stack [Fig. 1(d) inset] is calculated. This process is repeated for the three independent diffraction orders (D_{00}, D_{01}, and D_{10}), and the final reflectance spectrum is obtained from their linear superposition (see the Supplemental Material for detailed formulation [45]). The analytical reflectance minima are overlaid on the FDTD predictions as squares with dashed black lines in Fig. 1(d). In addition, the combined reflectance spectra for D_{01} and D_{10}, following the same approach, are calculated and their minima overlaid as circles with dashed green lines in Fig. 1(d). The splitting of modes takes place due to phase transition after excitation of the LSPR, which is evident

from the dispersion of energy density of different diffraction orders as a function of wavelength. The LSRP is suppressed by the simultaneous presence of the D_{00} FP (HW) mode between combined $(D_{00} + D_{01} + D_{10})$ modes on the dispersion diagram [Fig. 1(d)]. Because of the node formation (HW condition: $2k_{00z}L - \phi_{00F} - \phi_{00BM} = 2\pi m$) of the D_{00} mode on the top surface, the LSPR is suppressed (due to weak excitation), resulting in high reflection. Overall, there is excellent correspondence between FDTD predictions and the analytical model. Small discrepancies originate from the limitation of the effective medium approach when the wavelength is comparable to geometrical features. Also, because of the limitation of parameter retrieval process, we assumed the same effective index for the thin film under TM and TE polarization for all angles. This behavior is not present in the following diffractionless system where pattern features are smaller than the wavelength of interest.

The subdiffraction system is comprised of a cavity structurally similar to the previous one but with three key modifications: the metal is silver, the periodicity is 300 nm, and the hole diameter is 200 nm. Silver was chosen to avoid the strong interband absorption of gold around 300 to 550 nm while the decreased 2D grating period excludes higher diffraction orders above 450 nm wavelength range. As with the previous system, the LSPR is determined from the FDTD predicted absorption as $A(\lambda) = 1 - R(\lambda) - T(\lambda)$, for a patterned silver film attached to a dielectric layer ($n_d = 1.56$), as illustrated in the Fig. 2(a) inset. Experimental dispersion data for silver from Ref. [44] were used. Two absorption peaks are observed at 610 and 505 nm and represent higher order LSPR oscillations supported by the perforated film under asymmetric environment (air as superstrate and photoresist as substrate)
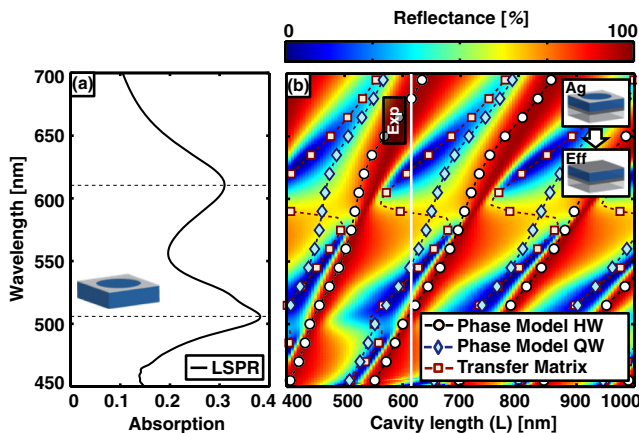

FIG. 2 (color online). Diffractionless plasmonic-cavity system. (a) FDTD predicted absorption spectrum showing two higher order LSPR absorption resonances at $\lambda = 511$ and 610 nm. (b) FDTD predicted cavity reflectance spectra. Analytical predictions from phase model and transfer matrix have been overlaid on top.

(Fig. S2, Supplemental Material [45]). Further addition of the silver back mirror completes the cavity-coupled system. The reflectance spectra are obtained by FDTD for cavity thicknesses ranging from 400 to 1000 nm and plotted in Fig. 2(b). As previously predicted, in the absence of diffraction, a single FP mode corresponding to the fundamental diffraction order is present with strong absorption enhancement around the LSPR wavelength (see Fig. S8 of the Supplemental Material [45] for a pictorial representation of the hybridization process). To understand the dispersion and explain the energy exchange mechanism between photonic and plasmonic modes, previously used approaches based on an analytical round-trip phase for QW condition [Eq. (1)] and transfer matrix method are followed. In both approaches the top perforated film is modeled by its corresponding effective medium retrieved following the aforementioned method. The first-order approximation based on a simple round-trip phase for QW condition predicts the overall dispersion and resonance locations with some degree of accuracy, as can be seen in Fig. 2(b) marked by diamonds with dashed blue lines. However, very good correspondence is observed for the transfer matrix case, marked by squares with dashed brown lines in Fig. 2(b), which includes every reflection and transmission event on all surfaces. As predicted, in a diffractionless scenario one can observe much closer agreement between numerical simulation and theoretical models. For the present symmetric plasmonic pattern, the polarization states play no role for the studied normal angle of incidence. However, for non-normal angle, the excitation of LSPR under TE and TM polarization will be different and the cavity phase matching condition will change. Such system configuration can be studied following the same technique laid down in the present Letter for normal angle of incidence.

To experimentally verify the above theoretical predictions, cavity-coupled plasmonic samples were fabricated following a nanotransfer printing technique reported in our earlier publications [49,50]. The top perforated metal pattern is grown on a patterned silicon stamp using electron beam deposition and then transfer printed to a polymer layer (SU-8) supported on a thick (200 nm) metal back mirror. A 50 nm thick sacrificial SiO_2 layer facilitates the release of the 30 nm thick gold and silver films from the silicon stamp for the diffraction and diffractionless cases, respectively. The corresponding SEM images are shown in Figs. 3(a) and 3(d). Reflectance spectra are measured using a microscope coupled Fourier transform infrared (FTIR) spectrometer (Hyperion 1000 - Vertex 80, Bruker Inc.) for cavity thicknesses $L = 610$ and 625 nm, Figs. 3(b) and 3(e), respectively. In both cases good agreement is observed between FDTD predictions and experimental measurements. Slight deviations originate from variations in cavity thickness, which is difficult to control via spin processing. In addition, numerical FDTD predicted cross
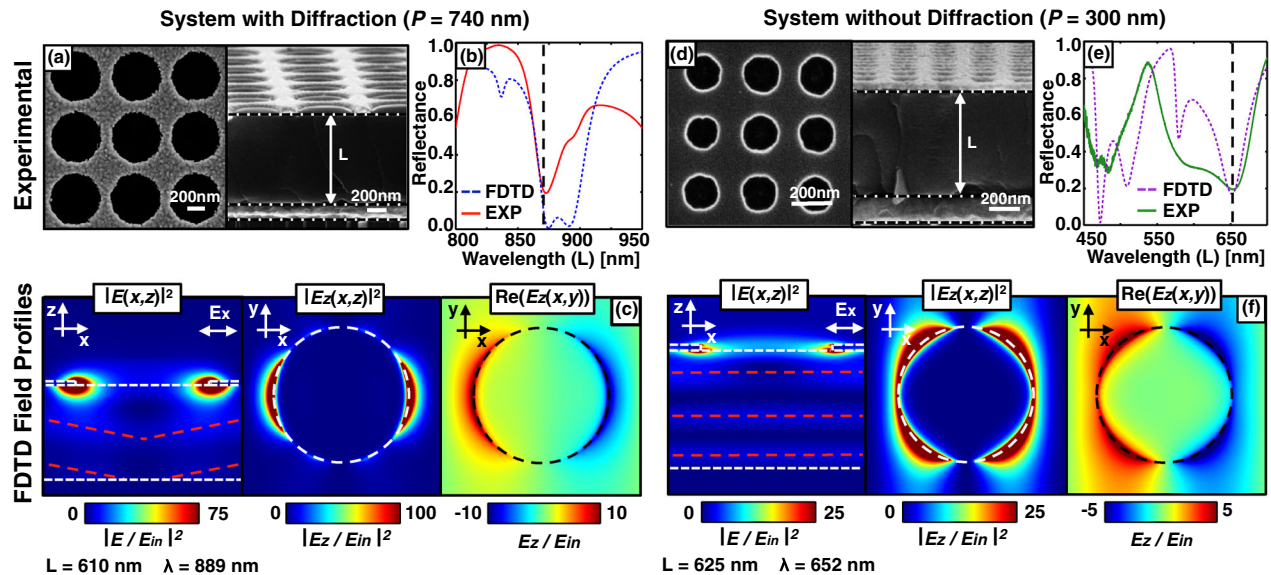
FIG. 3 (color online).   SEM image of fabricated (a) diffraction ($P = 740$ nm) and (d) diffractionless ($P = 300$ nm) cavity: top view (left) and cross sectional view (right). (b) FDTD predicted and experimentally measured reflectance spectrum for cavity thickness $L = 610$ nm for the $P = 740$ nm system. (c) The corresponding spatial field distribution at $\lambda = 889$ nm and $L = 610$ nm: cross section (left) and top (center) views of intensity distribution and top view of real part of E_z component (right). (e) FDTD and experimental reflectance spectrum for $L = 625$ nm for the $P = 300$ nm system. (f) The corresponding spatial field distribution at $\lambda = 652$ nm and $L = 625$ nm: cross section (left) and top (center) views of intensity distribution and top view of real part of E_z component (right).

sectional and top view intensity profiles at the strongest resonance points [dashed lines on Figs. 3(b) and 3(e)] are shown in Figs. 3(c) and 3(f), respectively, to show the combined plasmonic-photonic mode in the cavity. Slanted phase fronts (dashed red lines) inside the cavity of Fig. 3(c) (left) for the diffracting system ($P = 740$ nm) result from higher diffraction order in the resonating mode. Contrary to this, the diffractionless system ($P = 300$ nm) shows the fundamental D_{00} mode as a flat wave front within the cavity, Fig. 3(f) (left).

A photonic cavity interacting with a plasmonic system in diffraction and diffractionless regimes was studied. In both cases, independent (without diffraction) or combined photonic modes from intracavity multiple wave interference (with diffraction) interact with the plasmonic mode based on the cavity phase matching conditions. The thin metallic grating, being a weak absorber by itself, can demonstrate strong absorption due to the coherent feedback of the cavity when the electric field creates an antinode at the perforated film. The opposite situation arises, and the absorption is reduced drastically when the electric field forms a node at the perforated film. By exploiting the tunability of the LSPR with respect to the cavity resonance one can, for example, switch the on and off state of the absorption band by detuning the LSPR from the cavity resonance by the surrounding index change. The same effect can be achieved by shifting cavity resonances by manipulating the dielectric layer, which can be tunable based on physical variables such as pressure, heat, electric current, or electric field intensity. This leads to change in the propagation phase

inside the cavity and consequently shifts the photonic response to turn on (enhance) or turn off (suppress) the LSPR excitation. Contrary to conventional surface plasmon resonance sensors, which directly detect plasmon resonance shift, the proposed concept exploits the change in coupling between plasmonic and photonic modes, which enables independent tuning and detuning of two resonances. These sensing mechanisms will enable the development of newer classes of biological or chemical sensors exploiting this strong plasmonic-photonic coupling.

---

*debashis.chanda@creol.ucf.edu

[1] H. Raether, *Surface Plasmons on Smooth and Rough Surfaces and on Gratings*, (Springer-Verlag, Berlin, 1988).
[2] S. H. Chang, S. Gray, and G. Schatz, Opt. Express **13**, 3150 (2012).
[3] R. Wannemacher, Opt. Commun. **195**, 107 (2001).
[4] C. Sonnichsen, A. C. Duch, G. Steininger, M. Koch, G. Von Plessen, and J. Feldmann, Appl. Phys. Lett. **76**, 140 (2000).
[5] C. L. Haynes, A. D. McFarland, L. Zhao, R. P. Van Duyne, G. C. Schatz, L. Gunnarsson, J. Prikulis, B. Kasemo, and M. Käll, J. Phys. Chem. B **107**, 7337 (2003).
[6] J. J. Mock, D. R. Smith, and S. Schultz, Nano Lett. **3**, 485 (2003).

[7] K. T. Carron, W. Fluhr, M. Meier, A. Wokaun, and H. W. Lehmann, J. Opt. Soc. Am. B **3**, 430 (1986).

[8] L. Scarabelli, M. Coronado-Puchau, and J. J. Giner-Casares, ACS Nano **8**, 5833 (2014).

[9] G. P. Kumar, J. Nanophoton. **6**, 064503 (2012).

[10] L. B. Sagle, L. K. Ruvuna, J. A. Ruemmele, and R. P. Van Duyne, Nanomedicine **6**, 1447 (2011).

[11] E. Hendry, T. Carpy, J. Johnston, M. Popland, R. V. Mikhaylovskiy, A. J. Lapthorn, S. M. Kelly, L. D. Barron, N. Gadegaard, and M. Kadodwala, Nat. Nanotechnol. **5**, 783 (2010).

[12] C. Escobedo, A. G. Brolo, R. Gordon, and D. Sinton, Nano Lett. **12**, 1592 (2012).

[13] J. Anker, W. Hall, O. Lyandres, N. Shah, J. Zhao, and R. Van Duyne, Nat. Mater. **7**, 442 (2008).

[14] S. J. Tan, L. Zhang, D. Zhu, X. M. Goh, Y. M. Wang, K. Kumar, C.-W. Qiu, and J. K. W. Yang, Nano Lett. **14**, 4023 (2014).

[15] K. Kumar, H. Duan, R. S. Hegde, S. C. W. Koh, J. N. Wei, and J. K. W. Yang, Nat. Nanotechnol. **7**, 557 (2012).

[16] S. Yokogawa, S. P. Burgos, and H. A. Atwater, Nano Lett. **12**, 4349 (2012).

[17] Q. Chen, D. Chitnis, K. Walls, T. D. Drysdale, S. Collins, and D. R. S. Cumming, IEEE Photonics Technol. Lett. **24**, 197 (2012).

[18] T. Xu, Y.-K. Wu, X. Luo, and L. J. Guo, Nat. Commun. **1**, 59 (2010).

[19] A. Boca, R. Miller, K. M. Birnbaum, A. D. Boozer, J. McKeever, and H. J. Kimble, Phys. Rev. Lett. **93**, 233603 (2004).

[20] T. Schwartz, J. A. Hutchison, C. Genet, and T. W. Ebbesen, Phys. Rev. Lett. **106**, 196405 (2011).

[21] Y. Kaluzny, P. Goy, M. Gross, J. M. Raimond, and S. Haroche, Phys. Rev. Lett. **51**, 1175 (1983).

[22] T. W. Ebbesen, H. J. Lezec, H. F. Ghaemi, T. Thio, and P. A. Wolff, Nature (London) **391**, 667 (1998).

[23] L. Martín-Moreno, F. J. García-Vidal, H. J. Lezec, K. M. Pellerin, T. Thio, J. B. Pendry, and T. W. Ebbesen, Phys. Rev. Lett. **86**, 1114 (2001).

[24] Z. H. Tang, R. W. Peng, Z. Wang, X. Wu, Y. J. Bao, Q. J. Wang, Z. J. Zhang, W. H. Sun, and M. Wang, Phys. Rev. B **76**, 195405 (2007).

[25] H. Liu and P. Lalanne, Nature (London) **452**, 728 (2008).

[26] Y.-J. Bao, R.-W. Peng, D.-J. Shu, M. Wang, X. Lu, J. Shao, W. Lu, and N.-B. Ming, Phys. Rev. Lett. **101**, 087401 (2008).

[27] R. Ameling and H. Giessen, Laser Photonics Rev. **7**, 141 (2013).

[28] Z. Xi, Y. Lu, W. Yu, P. Yao, P. Wang, and H. Ming, Opt. Lett. **38**, 1591 (2013).

[29] J. Cesario, R. Quidant, G. Badenes, and S. Enoch, Opt. Lett. **30**, 3404 (2005).

[30] D. Chanda, K. Shigeta, T. Truong, E. Lui, A. Mihi, M. Schulmerich, P. V. Braun, R. Bhargava, and J. A. Rogers, Nat. Commun. **2**, 479 (2011).

[31] P. Jouy, Y. Todorov, A. Vasanelli, R. Colombelli, I. Sagnes, and C. Sirtori, Appl. Phys. Lett. **98**, 021105 (2011).

[32] R. Ameling, D. Dregely, and H. Giessen, Opt. Lett. **36**, 2218 (2011).

[33] L. Fu, P. Schau, K. Frenner, W. Osten, T. Weiss, H. Schweizer, and H. Giessen, Phys. Rev. B **84**, 235402 (2011).

[34] R. Taubert, R. Ameling, T. Weiss, A. Christ, and H. Giessen, Nano Lett. **11**, 4421 (2011).

[35] T. Weiss, N. A. Gippius, G. Granet, S. G. Tikhodeev, R. Taubert, L. Fu, H. Schweizer, and H. Giessen, Photonics and Nanostructures **9**, 390 (2011).

[36] A. Christ, S. G. Tikhodeev, N. A. Gippius, J. Kuhl, and H. Giessen, Phys. Rev. Lett. **91**, 183901 (2003).

[37] B. Auguié, X. M. Bendaña, W. L. Barnes, and F. J. García de Abajo, Phys. Rev. B **82**, 155447 (2010).

[38] L. Salomon, F. Grillot, A. V. Zayats, and F. de Fornel, Phys. Rev. Lett. **86**, 1110 (2001).

[39] H. F. Ghaemi, T. Thio, D. E. Grupp, T. W. Ebbesen, and H. J. Lezec, Phys. Rev. B **58**, 6779 (1998).

[40] R. W. Wood, Proc. Phys. Soc. London **18**, 269 (1902).

[41] A. Yariv and P. Yeh, *Photonics*, Optical Electronics in Modern Communications (Oxford University Press, New York, 2007).

[42] J. B. Pendry, L. Martín-Moreno, and F. J. Garcia-Vidal, Science **305**, 847 (2004).

[43] H. Shin, P. B. Catrysse, and S. Fan, Phys. Rev. B **72**, 085436 (2005).

[44] E. D. Palik, *Handbook of Optical Constants of Solids* (Academic Press, New York, 1998).

[45] See the Supplemental Material at http://link.aps.org/supplemental/10.1103/PhysRevLett.113.263902 for more information on field profiles, near- and far-field cavity dispersion, effective index calculation, and reflectance calculation using the transfer matrix approach.

[46] D. R. Smith, S. Schultz, P. Markoš, and C. M. Soukoulis, Phys. Rev. B **65**, 195104 (2002).

[47] X. Chen, T. M. Grzegorczyk, B.-I. Wu, J. Pacheco, and J. A. Kong, Phys. Rev. E **70**, 016608 (2004).

[48] C. Menzel, C. Rockstuhl, T. Paul, F. Lederer, and T. Pertsch, Phys. Rev. B **77**, 195328 (2008).

[49] D. Chanda, K. Shigeta, S. Gupta, T. Cain, A. Carlson, A. Mihi, A. J. Baca, G. R. Bogart, P. Braun, and J. A. Rogers, Nat. Nanotechnol. **6**, 402 (2011).

[50] L. Gao, Y. Kim, A. Vázquez-Guardado, K. Shigeta, S. Hartanto, D. Franklin, C. J. Progler, G. R. Bogart, J. A. Rogers, and D. Chanda, Adv. Opt. Mater. **2**, 256 (2014).